Grid Impedance Estimation During Large SCR Drop Events With Grid-Forming Converters

Citation for the original published paper (version of record):
Liu, W., Bongiorno, M., Narula, A. et al (2026). Grid Impedance Estimation During Large SCR Drop Events With Grid-Forming Converters. IEEE Transactions on Industrial Electronics, In Press.
http://dx.doi.org/10.1109/TIE.2026.3661054

Grid Impedance Estimation During Large SCR Drop Events With Grid-Forming Converters

Wentao Liu, *Member, IEEE*, Massimo Bongiorno, *Senior Member, IEEE*,
Anant Narula, *Member, IEEE*, and Jan R. Svensson, *Senior Member, IEEE*

***Abstract*—Grid-connected converters face significant synchronization challenges when suddenly exposed to ultraweak grid conditions, primarily due to the large and unknown grid impedance. This article proposes a passive method for efficiently estimating grid impedance during large short-circuit ratio (SCR) drop disturbances. The proposed method relies solely on local real-time measurements—specifically, voltage magnitude, active power, and reactive power at the point of common coupling (PCC)—to estimate fundamental grid impedance during transients. By leveraging the superior voltage control capability of grid-forming (GFM) converters, PCC voltage magnitude remains stable throughout the estimation process, thereby satisfying a requirement of the proposed approach. Furthermore, this method is inherently robust to grid frequency variations and phase angle jumps, further enhancing its practical applicability. With efficient impedance estimation, the converter can promptly adjust its active power reference to maintain synchronization. The effectiveness of this method has been validated through experimental results.**

***Index Terms*—Grid-forming (GFM) converter, grid impedance estimation, short-circuit ratio, ultraweak grid.**

I. INTRODUCTION

GRID-FORMING (GFM) control is a progressive alternative to conventional grid-following control in the operation of grid-connected converters, functioning as a crucial interface for diverse renewable energy sources [1]. This control approach provides notable benefits, particularly in terms of enhancing stability in weak grid conditions [2], [3] and providing robust support voltage and frequency amidst grid voltage dips [4] and frequency disturbances [5]. Generally, the fault ride-through control strategies are based on the premise that the transmission line can handle sufficient power transfer [6]. However, during disturbances that cause significant drops in short-circuit ratio (SCR), such as the disconnection of a major transmission line, the available power transfer capacity may fall below the active power output command set for the GFM converter before the disturbance. This situation can lead to an active power mismatch that threatens synchronization [7]. To accurately establish the new active power output, it is crucial to evaluate the power transfer capacity of the remaining transmission lines, which requires knowing the grid impedance following the disturbance.

To acquire real-time grid impedance information, three primary methods have been developed: active, quasi-passive, and passive estimation [8]. The first category involves the active injection of various nonfundamental frequency signals, such as low-frequency signal [9], [10], high-frequency signal [11], impulse signal [12], triangular-signal [13], pulsed-signal [14], [15], and pseudorandom binary sequence (PRBS) [16], [17], into the grid by the connected converters. The grid impedance is then estimated by analyzing the system's response to these injections. For instance, the estimation method presented in [9] and [10] utilizes a 75 Hz inter-harmonic current injection, which is subsequently analyzed using a fast Fourier transform (FFT) to assess the grid impedance. Similarly, a 630 Hz signal is used with a lower impact on the fundamental signals [11]. Apart from FFT, Alves et al. [11] employ wavelet transform (WT) for data analysis, offering a shorter processing time [19]. Mohammed and Ciobotaru [13] introduce two triangular pulses along the d- and q-axis, applying complex curve fitting to derive a wideband grid impedance and evaluate the system stability. Another wideband impedance estimation, achieved by pulse-train injection as described in [15], is suitable for both balanced and unbalanced grid conditions. However, it significantly degrades the output waveform quality during the estimation period. Compared with other kinds of active injection, the PRBS injection utilized in [16] produces less distortion at the converter output due to its digital approximation of white noise. However, this method tends to have a slower estimation speed and higher implementation complexity [18]. While active impedance estimation can

Received 15 May 2025; revised 29 August 2025, 5 November 2025, and 16 December 2025; accepted 21 January 2026. *(Corresponding author: Wentao Liu.)*

Wentao Liu, Massimo Bongiorno, and Anant Narula are with the Department of Electrical Engineering, Chalmers University of Technology, 41296 Göteborg, Sweden (e-mail: wentaol@chalmers.se; massimo.bongiorno@chalmers.se; anant.narula@chalmers.se).

Jan R. Svensson is with Hitachi Energy Research, SE-72226 Västerås, Sweden (e-mail: jan.r.svensson@hitachienergy.com).

Digital Object Identifier 10.1109/TIE.2026.3661054

function independently of natural grid disturbances, the additional frequency components introduced may degrade power quality and conflict with the grid codes [5]. Additionally, while active estimations are effective in steady-state conditions, their validation under large transient events remains to be explored.

In the second category, quasi-passive grid impedance estimation is achieved by actively introducing variations in the converter's active and reactive power references without the need for nonfundamental frequency signal injection. By performing multiple measurements at distinct operating points under stable grid conditions, such as two [20] or three steady-state operating points [21], the grid impedance is estimated by monitoring the PCC voltage. However, this approach requires several steady-state operating points for each estimation, making it challenging to implement during the SCR disturbances. Using continuous power pulses, Fantino et al. [22] proposed an observer that monitors the variables of the LCL filter to derive grid impedance, resulting in a THD of up to 5.1%. As an alternative, large PQ step responses can be used to perform fundamental grid impedance estimation during the power-tracking process of GFM converters [23]. However, this approach presupposes a stable grid frequency and ideal conditions without noise in the simulation verification. Conversely, in [24], Fang et al. proposed leveraging angle variations in the GFM controller to represent real power angle changes, allowing for impedance estimation with minimal PQ variations. However, this method assumes that the grid frequency is fixed without phase jumps, which may be challenging to apply in real-world conditions.

In the third category, the grid impedance estimation can be achieved by normal steady-state operation or natural system disturbances. Hence, this category can be further divided into two subsets, one of which is pure passive methods. Kalman filter-based observers are adopted to estimate the grid impedance without extra signal injection or changing operating points [25], [26]. However, tuning the parameters of the Kalman filter can be challenging [25]. Furthermore, the accuracy of the estimation is significantly affected by the grid conditions [26]. In the other subset, article [27] addresses scenarios involving a drop in grid SCR by employing a concept similar to that in [24]. When the estimated SCR falls below a certain threshold, the GFM controller is switched from PQ to PV mode to maintain stability. Nonetheless, this method is still based on a fixed grid frequency condition and only considers a minimum SCR of 1.5. Pepper and Campos-Gaona [7] investigated the ultraweak grid conditions and proposed a grid impedance estimation method by detecting the maximum active power operating point. However, this estimation carries a risk of instability, and despite validation through simulations, it remains unsuitable for practical applications.

Most existing estimation methods are developed for relatively strong grid conditions. However, in practice, the grid may experience a drastic SCR drop below 1, leading to the loss of the stable equilibrium point. The resulting mismatch between the reduced grid transfer capability and converter's preset setpoints can further cause loss of synchronization. To prevent this, the converter's active power setpoint must be promptly constrained, with limitation determined by the postdisturbance grid impedance. Nevertheless, an estimation method that remains effective during such severe SCR-drop transients is still lacking.

Motivated by this gap, this article proposes a robust grid impedance estimation method applicable during large SCR drop transients, relying solely on local measurements of real-time PCC voltage and output power. The proposed approach leverages the characteristic PQ trajectory, which inherently reflects the dynamic power transfer limits of the remaining transmission line. Moreover, the method remains effective under varying grid frequency and phase jumps, demonstrating strong practical applicability. The proposed approach is experimentally validated. The main contributions to this article are summarized as follows.

1) This article addresses grid impedance estimation during large SCR drops by introducing a simple and easily implementable passive approach that relies solely on local measurements. The method remains effective even under challenging grid conditions, including grid frequency variations and phase jumps.
2) With fast online grid impedance estimation, the active power reference of the GFM converter can be rapidly adjusted to maintain stability and prevent loss of synchronization.

II. FUNDAMENTALS

A. Basic GFM Control

To operate a GFM converter as a reliable voltage source behind an output inductor, this work adopts the virtual admittance (VA)-based GFM controller as described in [2] with the implementation depicted in Fig. 1. Measurements of active power (P_g), reactive power (Q_g), and PCC voltage (u_g) are fed into active power control (APC) loop and AC voltage control (AVC) modules and then generate the virtual-back EMF voltage u_{EMF}. APC has an active power reference limiter generating an upper limit of P_g, denoted as P_{ul}

$$P_{ul} = \sqrt{S_{\text{avail}}^2 - Q_g^2} \tag{1}$$

where $S_{\text{avail}} = S_{\text{rated}} U_g / U_{\text{rated}}$. U_g is the PCC voltage magnitude. S_{rated} and U_{rated} denote the nominal values of converter power and voltage, respectively, and are used as the base values for normalization. The limited active power reference $P_{\text{ref\_lim}}$ is obtained by passing the preset P_{ref} through the limiter. The angle reference θ_{EMF} for u_{EMF} is derived based on

$$\theta_{\text{EMF}} = \frac{1}{s}\left[(P_{\text{ref\_lim}} - P_g)\left(K_p + \frac{K_i}{s}\right) - R_a P_g + \omega_{\text{rated}}\right] \tag{2}$$

where K_p and K_i are the PI values of APC, R_a is an active-damping term, and ω_{rated} is the nominal angular speed. To generate the magnitude reference of u_{EMF}, the control law for the AVC, referring to [5], is utilized with a single integrator

$$U_{\text{EMF}} = U_{\text{rated}} + \frac{K_{iV}}{s}(U_{\text{ref}} - U_g - k_D Q_g) \tag{3}$$

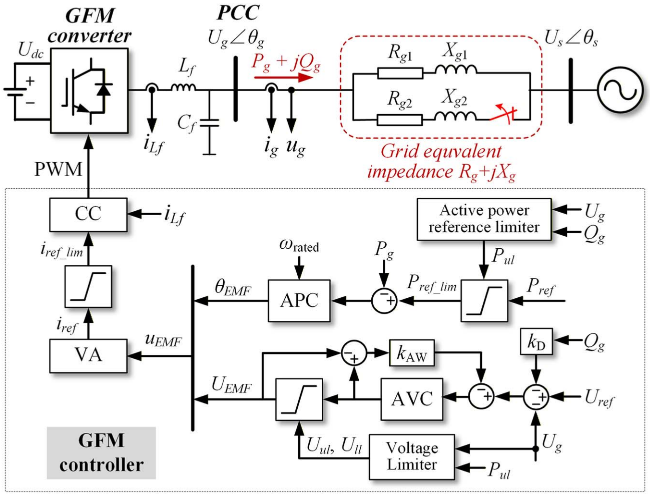

Fig. 1. Diagram of grid-forming converter with its control structure.

where K_{iV} and k_D are the integral gain and the droop constant of AVC, respectively. In addition, to prevent overcurrent, U_{EMF} is constrained by the upper and lower limits, given as

$$U_{ul} = \left|\boldsymbol{u_g} + \operatorname{conj}\left[\left(P_{ul} + j\sqrt{S_{\text{avail}}^2 - P_{ul}^2}\right)/\boldsymbol{u_g}\right](R_v + jX_v)\right| \tag{4}$$

$$U_{ll} = \left|\boldsymbol{u_g} + \operatorname{conj}\left[\left(P_{ul} - j\sqrt{S_{\text{avail}}^2 - P_{ul}^2}\right)/\boldsymbol{u_g}\right](R_v + jX_v)\right| \tag{5}$$

where $R_v + jX_v$ is derived from preset VA. The bold $\boldsymbol{u_g}$ denotes the vector expression of the PCC voltage. The VA-based current control module generates the converter output voltage reference for the PWM module. For more details on the GFM implementation, please refer to [5].

B. Loss of Synchronization With an Ultraweak Grid

To ensure stable GFM converter operation with full active power injection, the grid line transmission capability, $P_{\text{line\_max}}$, must exceed the converter's rated power. With grid equivalent impedance ($Z_g = R_g + jX_g$), the P_g can be represented as

$$P_g = \frac{U_g^2 R_g - U_g U_s R_g \cos\delta + U_g U_s X_g \sin\delta}{R_g^2 + X_g^2}. \tag{6}$$

From (6), assuming U_g and U_s are close to 1 p.u. and neglecting R_g, $P_{\text{line\_max}}$ (approximately $1/X_g$) is achieved when the power angle $\delta = (\theta_g - \theta_s) = \pi/2$. To describe the ultraweak grid condition, the definition of short-circuit ratio SCR is given

$$\text{SCR} = \frac{1}{Z_{g\_pu}} = \frac{1}{\sqrt{R_g^2 + X_g^2}/Z_b} \tag{7}$$

where Z_{g_pu} is the grid impedance in per-unit. The base impedance Z_b is defined as $U_{\text{rated}}^2/S_{\text{rated}}$. When a main transmission line trips unexpectedly, the SCR dramatically drops to a low value, potentially falling below the converter's nominal power, which may lead to a loss of synchronization. To illustrate this phenomenon, the P-δ curves with different SCRs are depicted in Fig. 2(a). The blue and red curves represent the P-δ curve with an SCR of 2 and 0.8, respectively. When SCR = 2, the $P_{\text{line\_max}}$ exceeds 1 p.u. Thus, the system can operate stably at the equilibrium operating point ***a***. When the SCR drops to 0.8, the operating point shifts from point ***a*** to point ***b***. Since the new $P_{\text{line\_max\_new}}$ is lower than the unchanged $P_{\text{ref}} = 1$, there is no equivalent point. The APC will continuously accelerate the frequency of u_{EMF}, ultimately resulting in a loss of synchronization. While the adaptive VA can enhance current limitations or transient performance [30], it does not affect the existence of stable equilibrium points under very weak grids. Therefore, a well-tuned constant VA providing sufficient damping is adopted in this work.

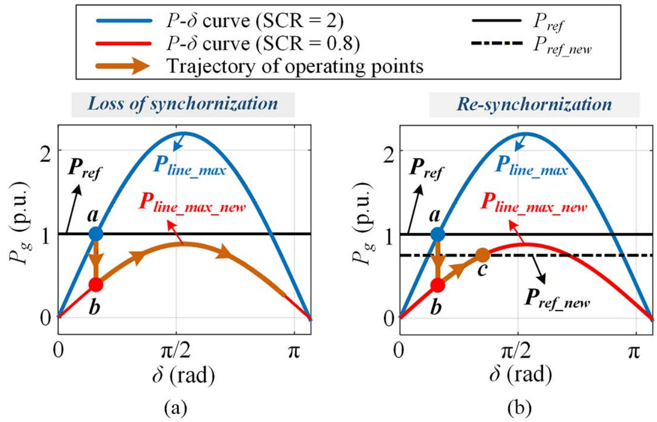

(a) (b)

Fig. 2. Diagram of P-δ curves when SCR decreases: (a) maintaining the constant active power reference P_{ref}; and (b) adjusting to a new active power reference $P_{\text{ref\_new}}$.

C. A Common Solution to Maintain Synchronization

While reducing active power injection to zero may temporarily maintain synchronization, it undermines the original goal of delivering available active power to prevent significant imbalances between power supply and demand. A better option is to determine a reasonably large active power reference while ensuring the angle stability [2]. To achieve this, the GFM controller must promptly complete the estimation of grid impedance and adjust its P_{ref}. As shown in Fig. 2(b), when the SCR decreases, and the active power reference is adjusted to $P_{\text{ref\_new}}$ (dashed black line), the system can be stable at the new equilibrium point ***c***.

Thus, the key to maintaining stability following a significant SCR drop is the rapid acquisition of grid impedance information. However, as indicated in (6), without knowing the real-time power angle, it is challenging to estimate Z_g directly. To address this, Section III presents the methodology for estimating grid impedance using local measurements during the SCR-drop transient period.

III. QUASI-POWER CIRCLE FITTING-BASED GRID IMPEDANCE ESTIMATION

A. Relationship Between P_g and Q_g Under Low SCR

As discussed, despite the rise in P_g observed during the transient in Fig. 2, the lack of real-time power angle complicates

TABLE I
COMPARISON OF DIFFERENT GRID IMPEDANCE ESTIMATION METHODS

Category of Estimation	References	Techniques	Estimation Duration	Design Complexity	Estimation Error	Suitable Scenarios
Active	[8]	Frequency sweeping	<60 s	Medium	Low	Steady state
	[12], [15]	Specific signal injection	<0.06 s	High	Low–Medium	Steady state
Quasi-passive	[20], [21]	Algebraic	∼0.1–1 s	Low	High	PQ reference variations
Passive	[25], [26]	Kalman filter	<0.1 s	High	Low–Medium	Steady state
	[23]	Algebraic	∼0.3 s	High	Medium	Large PQ transient
	Proposed	Quasi-power circle fitting	∼0.2 s	Medium	Medium	SCR drop transient

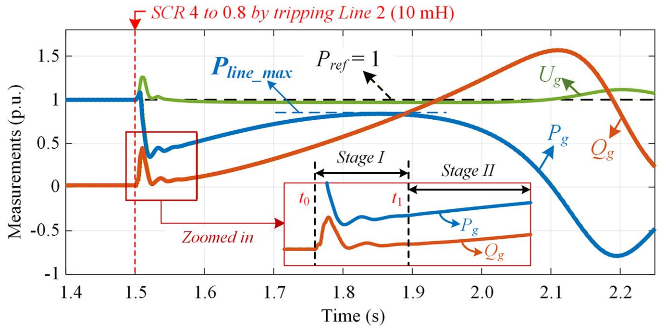

Fig. 3. Transient waveforms of active power, reactive power, and magnitude of PCC voltage when SCR decreases from 4 to 0.8.

deriving key system parameters. In addition to P_g, reactive power provides valuable insights, as a larger inductive grid impedance demands higher reactive power. Considering the inductive transmission line that $X_g \gg R_g$, the reactive power equation can be simplified as

$$Q_g = \frac{U_g(U_g - U_s\cos\delta)}{X_g}. \tag{8}$$

In a strong grid, the power angle δ remains small, and cos(δ) stays close to 1, making changes in voltage amplitude appear more pronounced. However, under ultraweak grid conditions, even if the voltage magnitude is stable, the APC significantly increases δ due to the mismatch of active power, resulting in a corresponding increase in Q_g. Meanwhile, the large variants in P_g and Q_g imply information about the power grid parameters.

Using the parameters in Table I and a grid impedance *R*/*X* ratio of 0.1, Fig. 3 illustrates the SCR drop transient waveforms of P_g, Q_g, and U_g at PCC. Note that the current limitation is disregarded here for clarity but is enabled in the subsequent experimental validation. At 1.5 s, the SCR decreases from 4 to 0.8 (tripping line 2 which has a 10 mH inductor and leaving only line 1 with a 40 mH inductor), causing the PCC voltage magnitude U_g (green curve in Fig. 3) to decrease slightly due to the droop control ($k_D = 0.01$ p.u.) and AVC bandwidth of 2.5 Hz [5]. However, PCC voltage U_g is still considered stable.

The active power reference P_{ref} (dashed black line) remains constant, exceeding the maximum active power $P_{\text{line\_max}}$ (blue dashed line) after the disturbance. Consequently, the converter cannot achieve equilibrium for P_{ref}, as discussed in Section II-B. The orange curve illustrates substantial fluctuations in Q_g following the SCR reduction, offering additional insights alongside the variations in P_g. An enlarged subfigure in Fig. 3 illustrates that the transient can be divided into two stages. Stage I features power oscillations, which can be regarded as electromagnetic transients; these power oscillations are stabilized quickly due to the effective design of the GFM controller. In stage II, power oscillations are negligible, and the stable change of power output becomes the primary focus of this article. As the power angle gradually increases, the operating points can be regarded as semisteady states [7], and the expressions P_g and Q_g follow (6) and (9). To maintain rigor, the full equation of reactive power transfer between PCC and remote grid voltage is given by

$$Q_g = \frac{U_g^2 X_g - U_g U_s R_g \sin\delta - U_g U_s X_g \cos\delta}{R_g^2 + X_g^2}. \tag{9}$$

Assuming that the postdisturbance grid impedance remains constant but unknown, the power equations in (6) and (9) can be reformulated using the parameter definitions in (12) to demonstrate the symmetry between P_g and Q_g [2]

$$P_g = \alpha U_g^2 - U_g U_s(\alpha\cos\delta - \beta\sin\delta) \tag{10}$$

$$Q_g = \beta U_g^2 - U_g U_s(\alpha\sin\delta + \beta\cos\delta) \tag{11}$$

$$\alpha = R_g/|Z_g|^2,\ \ \beta = X_g/|Z_g|^2,\ \ |Z_g| = \sqrt{R_g^2 + X_g^2}. \tag{12}$$

Note that parameters α and β are constant. However, the power angle δ is hardly obtained in real-time operation. To eliminate δ, based on (10) and (11), the relationship between P_g and Q_g can be further derived as

$$(P_g - \alpha U_g^2)^2 + (Q_g - \beta U_g^2)^2 = (U_g U_s/|Z_g|)^2. \tag{13}$$

B. Grid Impedance Estimation Based on the Local Measurements

From (13), if the voltage magnitudes U_g and U_s remain constant, the trajectory of P_g and Q_g forms a perfect circle with a center at $(\alpha U_g^2, \beta U_g^2)$ and a radius of $U_g U_s/|Z_g|$. However, during a transient event, the PCC voltage magnitude U_g is not perfectly constant, which causes variations in both the circle center and radius. Specifically, the circle center coordinates are proportional to U_g^2, making them highly sensitive to voltage fluctuations. To mitigate the quadratic dependency and account for the unit, (13) is reformulated as

$$\left(\frac{P_g Z_b}{U_g^2} - \alpha Z_b\right)^2 + \left(\frac{Q_g Z_b}{U_g^2} - \beta Z_b\right)^2 = \left(\frac{U_s Z_b}{U_g|Z_g|}\right)^2. \tag{14}$$

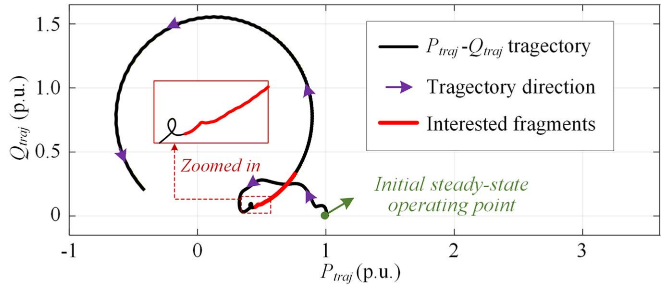

Fig. 4. Trajectory of P_{traj} versus Q_{traj} when SCR decreases from 4 to 0.8.

Equation (14) defines a circle, referred to as the quasi-power circle C_{qp}, with its center at $(\alpha Z_b, \beta Z_b)$ and a radius of $(Z_bU_s)/(U_g/|Z_g|)$. The circle center is determined by the true grid impedance and remains fixed when the grid equivalent impedance does not changed after the transient SCR drop. Although the radius still depends on U_g, its dependence remains first order, so no additional error is introduced into the fitting process. Therefore, the overall impact of U_g variations on the circle fitting is significantly reduced, improving the estimation accuracy. Furthermore, to achieve normalization, (13) is scaled by multiplying both sides by z_b^2. By recording a sufficient number of quasi-power trajectory points of (P_{traj}, Q_{traj}) as defined in

$$\begin{cases} P_{\text{traj}} = P_g Z_b / U_g^2 \\ Q_{\text{traj}} = Q_g Z_b / U_g^2. \end{cases} \tag{15}$$

The parameters of circle C_{qp} can be obtained through an appropriate fitting algorithm. Using the data in Fig. 3, the trajectory of (P_{traj}, Q_{traj}), labeled in black, is shown in Fig. 4. After the SCR reduction disturbance, the operating point shifts from the initial point of (1, 0) to around (0.4, 0) and continuous along the path indicated by the purple arrows, delineated a circular pattern on the plane, as described by (14). Note that the operating point initially deviates from the power circle due to significant variations in the PCC voltage magnitude and subsequently shifts toward the expected location as the voltage stabilizes. Therefore, by fitting a circle to the prominent segment (illustrated by the red curve in Fig. 4), the center of the circle, directly related to the grid impedance, can be accurately estimated. Assuming the center of circle C_{qp} (x_{c_fit}, y_{c_fit}), is fitted, the grid impedance can be ultimately estimated using (14) as follows:

$$\begin{cases} R_{g\_\text{est}} = x_{c\_\text{fit}} Z_b / x_{c\_\text{fit}}^2 + y_{c\_\text{fit}}^2 \\ X_{g\_\text{est}} = y_{c\_\text{fit}} Z_b / x_{c\_\text{fit}}^2 + y_{c\_\text{fit}}^2. \end{cases} \tag{16}$$

Therefore, precise quasi-power circle fitting is essential, as will be demonstrated in Section III-C.

C. Quasi-Power Circle Fitting

The numerical equation for (14) can be derived through circle fitting with real-time measurements of (P_{traj}, Q_{traj}) based on the following assumptions.

1) After an SCR reduction disturbance, the grid impedance remains constant during the transient process.
2) The PCC voltage magnitude U_g is steadily controlled (though not necessarily at its rated value) while the grid voltage magnitude U_s remains stable during the transient.
3) The GFM controller is well tuned, providing effective damping against the SCR reduction disturbance, ensuring small-signal stability in the system.

Note that although a circle can theoretically be calculated with three noncollinear points, noise in real systems degrades measurements, so using multiple samples leads to a more precise fit. Additionally, as shown in Fig. 3, a sudden shift to ultraweak grid conditions causes a rapid drop in P_g, which serves as an initial indicator of grid structural changes [11], [23]. When the drop in P_g, denoted ΔP_g, exceeds a preset threshold ΔP_{th}, measurements are triggered, making the timestamp t_0 in Fig. 3. When the system enters stage I, noticeable transient power oscillations occur, which should be monitored until they subside. A method to determine the timestamp t_1 involves comparing the measured (P_{traj}, Q_{traj}) with their sliding-window averages. The sum of squared errors between pre- and postfiltered (P_{traj}, Q_{traj}) values is computed

$$\text{Err}_{\text{stageI}} = \sum \left[(P_{\text{traj}} - P_{\text{traj\_ave}})^2 + (Q_{\text{traj}} - Q_{\text{traj\_ave}})^2 \right] \tag{17}$$

where $P_{\text{traj\_ave}}$ and $Q_{\text{traj\_ave}}$ represent the sliding window filtered values of P_{traj} and Q_{traj}, respectively. After $\text{Err}_{\text{StageI}}$ falls below a preset threshold at timestamp t_1, the algorithm records a series of (P_{traj}, Q_{traj}) points, referred to

$$x_k = P_{\text{traj}}(k), \quad y_k = Q_{\text{traj}}(k) \tag{18}$$

where the subscript k denotes the kth recorded data point in the time domain, with x_k and y_k forming a set of coordinates. Given that n sets of coordinates are recorded, two matrices X and Y can be constructed as follows:

$$X = \begin{bmatrix} 2x_1 & 2y_1 & 1 \\ 2x_2 & 2y_2 & 1 \\ \vdots & \vdots & \vdots \\ 2x_n & 2y_n & 1 \end{bmatrix}_{n\times 3} \qquad Y = \begin{bmatrix} -x_1^2 - y_1^2 \\ -x_2^2 - y_2^2 \\ \vdots \\ -x_n^2 - y_n^2 \end{bmatrix}_{n\times 1}. \tag{19}$$

The relationship between matrices X and Y is given by

$$Y = X\lambda + \varepsilon \tag{20}$$

where λ is a three-element column vector, $[\lambda_1, \lambda_2, \lambda_3]^T$, containing the parameters required for fitting the quasi-power circle, and ε represents the error term. To minimize the sum of squared residuals $\|\varepsilon\|_2$, the least squares method can be applied. Therefore, λ can be estimated using

$$\lambda = \arg\min \|\varepsilon\|_2^2 = (X^TX)^{-1}(X^TY). \tag{21}$$

Based on the estimated λ, the center of the circle C_{qp} can be calculated as follows:

$$\begin{cases} x_{c\_\text{fit}} = -\lambda_1 \\ y_{c\_\text{fit}} = -\lambda_2. \end{cases} \tag{22}$$

D. Further Refinement of Quasi-Power Circle Fitting Implementation

1) Recursive Least Squares: Section III-C presents a clear process of fitting quasi-power circle C_{qp}, but it requires all measurements, increasing online computational and memory demands. To reduce this burden, the recursive least squares (RLSs) method is employed [28]. This approach updates the current fitting result using new measurements while retaining some information from the previous data by adjusting the forgetting factor λ_{FF}. In addition, the RLS algorithm prioritizes newly collected data. Hence, it is not necessary to pinpoint the exact start time of stage II. Instead, incorporating an appropriate time delay unit is a straightforward approach to bypass the initial stage I. The RLS-based circle-fitting algorithm is directly given by

$$\begin{cases} X_k = [2x_k, 2y_k, 1] \\ Y_k = -x_k^2 - y_k^2 \\ K_k = \frac{P_{k-1}X_k}{\lambda_{FF}+X_k^T P_{k-1} X_k} \\ \lambda_k = \lambda_{k-1} + K_k(Y_k - X_k^T \lambda_{k-1}) \\ P_k = (P_{k-1} - K_k X_k^T P_{k-1})/\lambda_{FF} \end{cases} \tag{23}$$

where subscript k denotes the variables at the kth iteration; and K_k and P_k are the kth correction matrix and covariance matrix, respectively. For further details on the RLS algorithm, please refer to [28].

2) Additional Information for Circle Fitting: Furthermore, Section II-B notes that the theoretical analysis of SCR reduction transient neglects the effects of current limits and grid voltage phase jumps. For instance, rapidly increasing reactive power that pushes the current close to its limit, triggering current saturation, may violate the second assumption in Section III-C, which pertains to the stable control of the PCC voltage amplitude. The limited effective measurements of the arc with a small central angle are not enough for an accurate circle fitting. To increase the effective central angle of the measured arc and expedite the fitting process, an additional virtual quasi-power point (x_0, y_0) near the circle C_{qp} is also considered. When the power angle is close to 0, i.e., $P_{\text{traj}} = 0$, the corresponding x_0 is 0, according to (18). It follows from (14) that

$$y_0 = \text{SCR}\left(\frac{X_g}{|Z_g|} - \sqrt{\left(\frac{U_s}{U_g}\right)^2 - \left(\frac{R_g}{|Z_g|}\right)^2}\right). \tag{24}$$

Given that the grid impedance is primarily inductive ($X_g \gg R_g$) and U_g and U_s are close to the system's nominal voltage, y_0 is approximately 0. Since this virtual point (0, 0) may not lie precisely on the fitted circle, its weight factor α_v within the fitting can be suitably reduced. Compared with (23), the algorithm differs, as shown

$$K_k = \frac{P_k X_0}{\lambda_{FF}/\alpha_v + X_0^T P_k X_0} \tag{25}$$

where $X_0 = [0, 0, 1]$, $Y_0 = 0$.

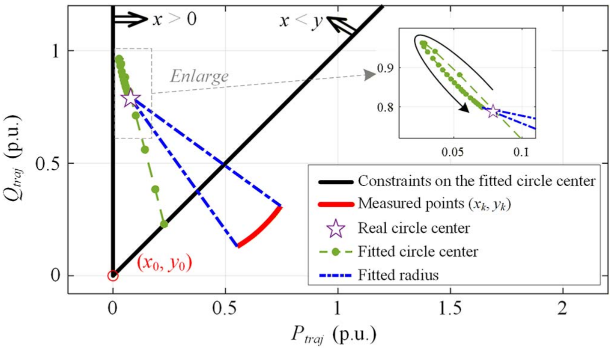

Fig. 5. Diagram of quasi-power circle fitting.

3) Constraints on the Fitting Circle Center: When using the RLS algorithm with partial measurements in stage I, as mentioned in Section III-D1, the fitted circle center may converge to an incorrect position due to transient power oscillations in stage I. Based on the physical interpretation of the true quasi-power circle center of (14), (αZ_b, βZ_b), where both coordinates are positive, and the grid transmission line is typically inductive (i.e., $X_g > R_g$), the estimated circle center is subject to the following constraint:

$$y_{c\_\text{est}} > x_{c\_\text{est}} > 0. \tag{26}$$

Therefore, the fitting algorithm begins to check for convergence only when the center of the fitted circle lies within the constraint range.

4) Determine the Completion of the Circle Fitting: The quasi-power circle fitting process is illustrated in Fig. 5, where the red curve represents the collected measurements; the black lines indicate the constraints on the fitted circle center; the purple star denotes the true circle center from (14) and the green dots along with the dashed line represent the trajectory of the fitted circle centers (in the enlarged subfigure, the black arrow indicates the direction of change for the fitted circle center). Although the true circle center is unknown, it is evident that the fitted circle center approaches the true center as more measurements are collected. When the fitted circle center stabilizes at a certain position and no longer obviously changes with new measurements input, the algorithm terminates the fitting process and provides the grid impedance estimation based on (16). The convergence of the circle fitting is indicated by the variance between the newly fitted circle center ($x_{c\_fit}[k]$, $y_{c\_fit}[k]$) and the M previously fitted centers, expressed as follows:

$$\begin{aligned} \text{Var}_{\text{cc}} = \frac{1}{M}\sum_{i=1}^{M}[(x_{c\_\text{fit}}[k] - x_{c\_\text{fit}}[k-i])^2 \\ + (y_{c\_\text{fit}}[k] - y_{c\_\text{fit}}[k-i])^2]. \end{aligned} \tag{27}$$

When the real-time calculated variance of the fitted circle center Var_{cc} is below the preset threshold Var_{th}, the circle-fitting process is terminated. Note that the final fitted circle center may not precisely align with the true center, resulting in a slight error due to the nonideal constant PCC voltage magnitude.

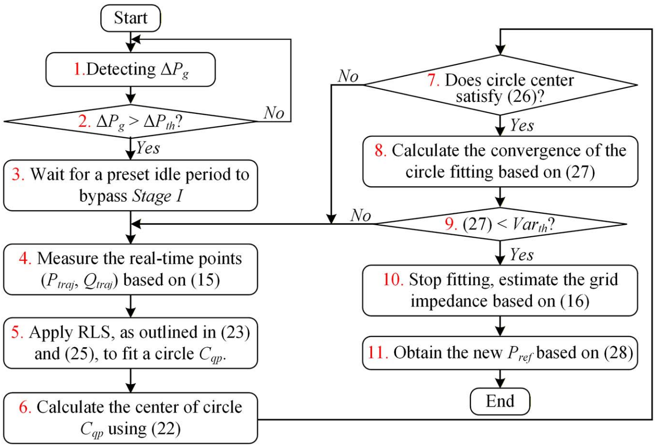

Fig. 6. Flowchart of circle fitting-based grid impedance estimation and New P_{ref} calculation.

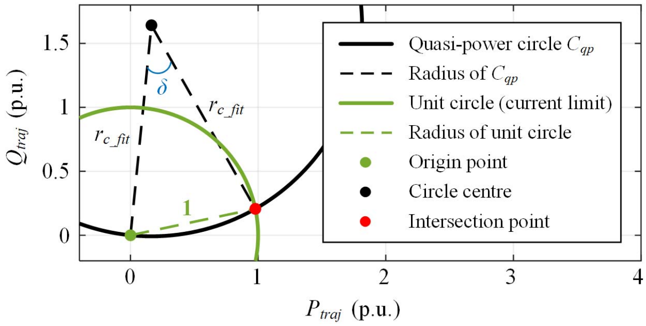

Fig. 7. Geometric relationship between the quasi-power circle and the unit circle representing 1 p.u. current limitation.

E. New Active Power Reference Selection With Estimated Grid Impedance

By combining (13) with the obtained grid impedance in (16) and assuming a stable grid voltage amplitude of around 1 p.u., the maximum active power transfer capacity ($P_{\text{line\_max}}$) of the postdisturbance grid is calculated as follows:

$$P_{\text{line\_max}} = \frac{R_{g\_\text{est}}}{|Z_{g\_\text{est}}|^2} U_g^2 + \frac{1}{|Z_{g\_\text{est}}|} U_g. \tag{28}$$

To maintain a certain angle stability margin, 0.85 times $P_{\text{line\_max}}$ can be selected as an example to be a new active power reference for low SCR conditions. Note that (1) dynamically ensures that the converter output current does not exceed 1 p.u., which is always enforced. Therefore, the final active power reference, $P_{\text{ref\_lim}}$, introduced into APC also depends on P_{ul}. It is noted that the active power reference correction is particularly effective when the postdisturbance SCR is lower than 1. Otherwise, the calculated new active power setpoint would exceed the inherent active power limiter P_{ul} and the latter determines the final active power reference. Fig. 6 provides a flowchart summarizing the proposed circle-fitting-based grid impedance estimation and subsequent P_{ref} correction.

It is worth noting that the proposed method is triggered by a drop in active power output. When the SCR recovers, the increase in active power does not trigger the estimation algorithm. Nevertheless, the converter can maintain synchronization since the strong grid naturally provides a stable equilibrium operating point. In such cases, nominal active power recovery can be coordinated according to grid operator requirements and grid codes.

F. Discussion on Method Applicability and Limitations

1) Adaptation to Nonideal Grid Source: The proposed quasi-power circle fitting-based grid impedance estimation requires only that the system meets the criteria listed in Section III-C, without the need for a constant grid frequency or continuous grid phase angle. Since grid frequency changes mainly affect the relative angular speed difference between the GFM converter and the grid, influencing the rate of power angle increase, and grid phase angle jumps only alter the start point of the circular movement, they do not affect the quasi-power trajectory as the power angle grows. Thus, even during the SCR reduction transient with dynamic grid frequency variations and phase angle jumps, the method can still accurately estimate the grid impedance.

Moreover, the proposed method remains applicable under nonnominal grid voltage conditions due to the inherent property of the quasi-power circle: its center depends solely on the grid impedance and remains fixed regardless of voltage magnitude. Therefore, as shown in (14), the circle radius varies with the grid voltage, and the accurate estimation of the stable circle center ensures reliable impedance calculation. However, since the quasi-power circle no longer passes through the origin under voltage deviations, the virtual operating point at (0, 0), which is derived based on the assumption of nominal voltage, is excluded from the fitting process. The corresponding validation is presented in Section IV-D.

2) Targeted Use in Low SCR Situations: The proposed grid impedance estimation relies on variations in both P_g and Q_g. However, when the postdisturbance SCR is relatively high, changes in the P_g injection have a minimal impact on Q_g variants. Based on (14), when SCR is high, the radius of circle C_{qp} is much larger than the collected arc segment, resulting in a small center angle. The SCR upper limit for this estimation method can be determined based on the geometric relationship between the fitted quasi-power circle and the rated current limitation shown in Fig. 7, where the central angle is as follows:

$$\delta = \arccos\left(\frac{2r_{c\_\text{fit}}^2 - 1}{2r_{c\_\text{fit}}^2}\right). \tag{29}$$

Assuming a minimal center angle of 30° (as an approximate threshold to illustrate the applicability limit of this method), the maximum estimated r_{c_est} is around 1.93 [i.e., SCR $\approx$ 1.93 according to (6) and (14)]. However, due to PCC voltage stability and measurement quality during the estimation, this theoretical SCR upper limit may be slightly lower in practice.

Additionally, grid impedance estimation is generally not required when SCR is greater than 1, as converters can typically maintain stable operation and inject full power without relying on it. Nevertheless, even in such strong grid conditions, grid impedance estimation can still provide additional benefits, such as enabling adaptive control strategies [9]. However, under ultraweak grid conditions (SCR < 1), accurate grid impedance estimation becomes crucial. In this case, even a robust converter design may still fail to maintain stable operation if no equilibrium exists. The proposed estimation method enables determining a correct new active power reference based on the actual grid strength, which not only helps maintain synchronization but also ensures that the available transmission capacity of the weak grid is fully utilized without causing instability. The proposed method is well suited for this scenario, further highlighting its practical value and necessity.

3) Comparison, Extensions, and Future Work: To better illustrate the performance related to other existing methods, a comparison is provided in Table I. Active grid impedance estimation methods using intrusive signal injections are typically faster and more accurate but impose higher computational costs. Among passive methods, Kalman filter-based observers offer rapid response but require complex design and parameter tuning. The transient measurement-based methods achieve slower estimation with moderate accuracy. Quasi-passive methods generally take longer and exhibit noticeable errors, as they only rely on a few steady-state operating points.

Although the proposed method has an applicable SCR upper limit, as discussed in Section III-F2, it could be extended to a wider SCR range if additional grid-side information is available. For instance, when the grid impedance ratio $R/X = K$ is known, the center of the quasi-power circle C_{qp} lies on the straight line $y = 1/Kx$. By exploiting the symmetry of C_{qp} about this line, the effective fitting center angle can be increased, enabling the estimation algorithm to operate under higher SCR conditions. However, because reactive power variation to the power angle becomes limited in strong grids, the proposed method remains best suited for weak grid conditions.

Furthermore, the proposed method is potentially applicable to converters capable of maintaining stable PCC voltage and is not strictly limited to grid-forming control. Nevertheless, grid-forming converters are adopted here due to their superior performance under very weak grid conditions. Extending the method to scenarios with varying PCC voltage represents an interesting direction for future research.

IV. VALIDATION AND COMPARISON

The proposed grid impedance estimation under ultraweak grid conditions is tested in an experimental setup shown in Fig. 8. The grid is emulated with a REGATRON four-quadrant programmable AC power source. The grid SCR reductions are completed by disconnecting one of two parallel impedances (for instance, line 1 with a 40 mH inductor remains, and line 2 with a 10 mH inductor is tripped). A two-level GFM converter is controlled by the ds1006 platform of dSPACE. The DC side of the converter is powered by an ideal DC source, while the AC side connects to the grid impedance through an LC filter. System and control parameters are specified in Table I.

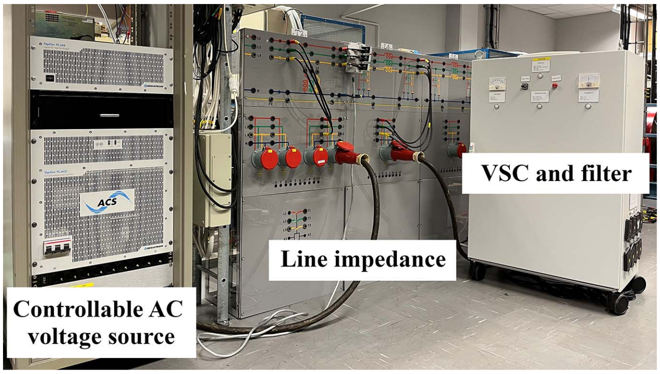

Fig. 8. Photo of laboratory setup.

A. Instability With Constant Active Power Reference

Initially, the system operates with two parallel lines, and the SCR is about 4. At t = 1.5 s, line 2 tripped, resulting in the SCR dropping to 0.8. Three-phase PCC voltage and converter output current are plotted in Fig. 9(a) and (b), respectively, with enlarged views highlighting the transient waveforms during the early stage of the disturbance. Thanks to the well-damped GFM control, the PCC voltage magnitude remains stable despite large SCR variations. The increased grid impedance causes reductions in the output current and active power injection P_g, as shown in Fig. 9. The difference between P_g and its limited reference $P_{\mathrm{ref\_lim}}$ prompts the APC controller to accelerate the converter frequency, as seen in the frequency curve in Fig. 9(d). As the power angle increases, both P_g and Q_g in Fig. 9(c) exhibit a similar upward trend as depicted in Fig. 3. Different from the simulation results shown in Fig. 3, an effective current limiting is implemented in the experiments, the constant P_{ref} (equals 1 p.u.) is limited by (1), resulting in the dynamic limited $P_{\mathrm{ref\_lim}}$ (curve in green) in Fig. 9(c). When $P_{\mathrm{ref\_lim}}$ is below 0.5, P_{ref} is set to 0 [5]. Despite P_{ref} being constrained, the system still exhibits transient instability following a significant SCR drop. Therefore, during the transient period, it is essential to promptly obtain a correct new active power reference $P_{\mathrm{ref\_new}}$. It is worth noting that the PCC voltage magnitude remains stable during the early transient, e.g., 1.5–1.9 s in Fig. 9(a), which meets the requirement of the proposed grid impedance estimation listed in Section III-C.

B. Grid Impedance Estimation Assisted Operation

Under the same disturbance condition, where the SCR drops to 0.8, the corresponding validation of grid impedance estimation is presented in Fig. 10. Unlike in Fig. 9, the estimation algorithm starts running following the process outlined in Fig. 6 after detecting the disturbance by monitoring the P_g drop with a preset threshold $\Delta P_{\mathrm{th}} = 0.1$ p.u. As the power angle increases, more points (P_{traj}, Q_{traj}) are measured, and the fitting circle center gradually converges to a constant, as depicted in Fig. 10(e). Based on (20), the grid impedance is estimated to be $(0.95 + j12.97)\,\Omega$, which closely matches the actual value of the applied 40 mH inductor. It can be observed that the estimation takes only around 0.2 s to produce an accurate result, demonstrating

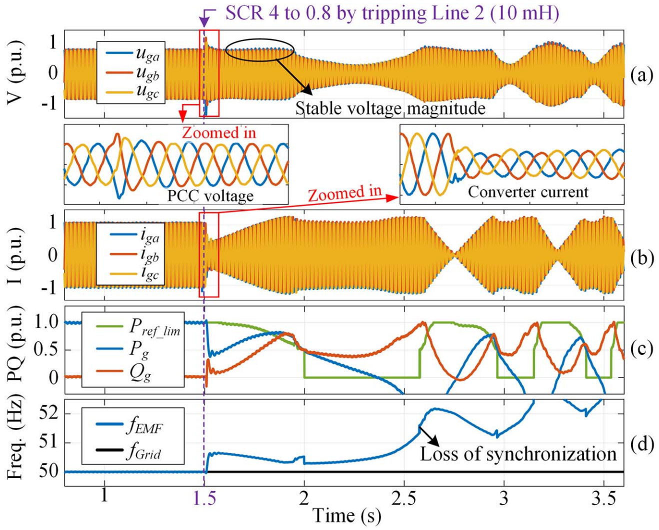

Fig. 9. Experimental unstable transient after a large SCR drop: (a) three-phase PCC voltage; (b) three-phase converter current; (c) limited active power reference, active and reactive power; and (d) frequency of GFM converter and the grid.

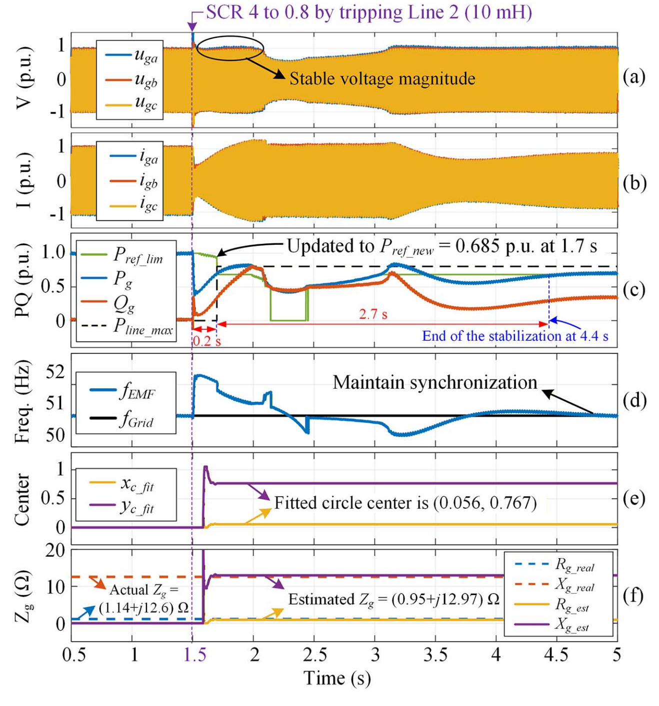

Fig. 10. Experimental results of grid-impedance estimation and stable transient after a large SCR drop: (a) three-phase PCC voltage; (b) three-phase converter current; (c) limited active power reference, active and reactive power; (d) frequency of GFM converter and the grid; (e) fitted circle center; and (f) actual and estimated grid impedance.

excellent performance. Based on (28), $P_{\text{line\_max}}$ is 0.806 p.u., shown as a black dashed line in Fig. 10(c). To maintain stability, the new active power reference, $P_{\text{ref\_new}}$, is selected as $0.85 \times P_{\text{line\_max}}$ and updated at 1.7 s, as indicated by the green curve in Fig. 10(c). Corresponding to the newly calculated $P_{\text{ref\_new}}$, the system reaches a new steady-state point after the transient process, at around 4.4 s. This moment is marked as the end of the stabilization.

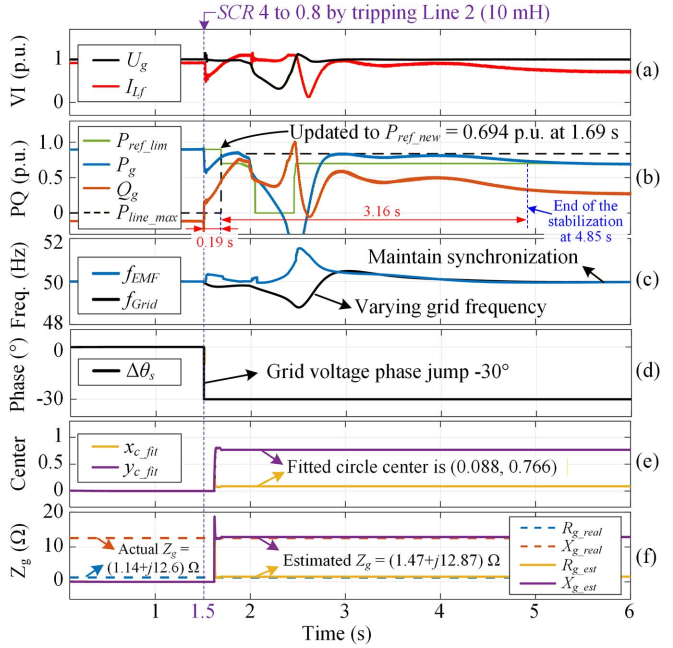

Fig. 11. Experimental results of grid-impedance estimation and stable transient after a large SCR drop with varying grid frequency and phase jump: (a) magnitudes of PCC voltage and converter current; (b) limited active power reference, active and reactive power; (c) frequency of GFM converter and the grid; (d) grid voltage phase jump; (e) fitted circle center; and (f) actual and estimated grid impedance.

On the other hand, to demonstrate the effectiveness of the proposed estimation method under nonideal grid conditions, the validation with a varying grid frequency and a power angle phase jump $\Delta\delta$ is conducted. The grid frequency variation is implemented based on the active power fluctuation. When the grid source detects a power disturbance, a voltage phase shift of $-30°$ is applied to create a $\Delta\delta$. The obtained results are shown in Fig. 11.

Grid SCR still drops at 1.5 s. Due to the active power change in the system, grid frequency varies, plotted as the black curve in Fig. 11(c). The added grid voltage phase shift is shown in Fig. 11(d), where the power angle jumps at 1.5 s. After a short period, the fitted circle center in Fig. 11(e) converges to a constant, and the corresponding grid impedance estimation is computed as shown in Fig. 11(f), which perfectly aligns with the real grid impedance value. Then, by adjusting the corrected new active power reference, the system ultimately maintains synchronization after a transient process, at around 4.85 s, which is marked as the end of the transient. In addition, the undesirable reverse active power phenomenon peaks at 0.77 p.u. of absorbed power in Fig. 11 and relatively slow dynamic responses both in Figs. 10 and 11, indicating that merely adjusting the active power setpoint is insufficient to ensure smooth transients under severe grid conditions. To effectively mitigate this issue, further enhancement of the GFM controller, such as adaptive APC, is necessary. While this article focuses on the proposed grid impedance estimation method, future work will systematically investigate advanced GFM control strategies

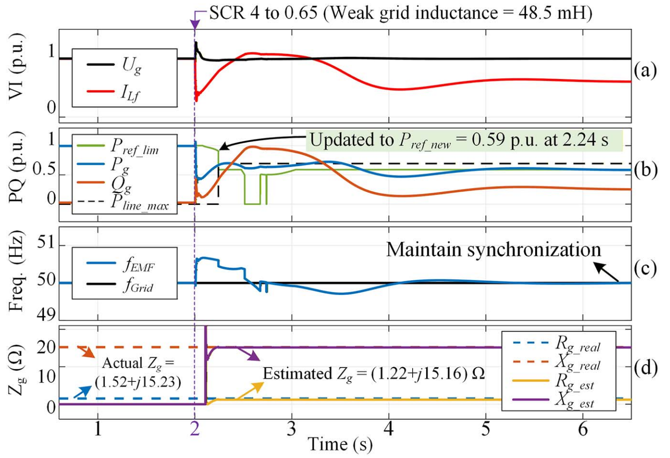

Fig. 12. Simulation results of grid-impedance estimation applying the proposed method under very low SCR conditions: (a) magnitudes of PCC voltage and converter current; (b) limited active power reference, active and reactive power; (c) frequency of GFM converter and the grid; and (d) actual and estimated grid impedance.

that incorporate knowledge of the grid impedance estimation to improve dynamic performance and stability.

To assess the effectiveness of the proposed method, an extreme condition of a reduction of SCR down to 0.65 is considered here, and the corresponding case study results are summarized in Fig. 12. With such a low SCR, no stable equilibrium point exists without adjusting the active power reference P_{ref}. The proposed method accurately estimates the grid impedance as $(1.22 + j15.16)$ Ω and reduces P_{ref} accordingly, thereby maintaining synchronization.

C. Grid Impedance Estimation Under Varying R/X Ratio

To further validate the effectiveness of the proposed grid impedance estimation method under different grid R/X ratios, a comparison case study with $R/X = 0.2$ is conducted using the simulation model and the same system parameters listed in Table I. The corresponding estimation results are presented in Fig. 13. The grid SCR drops to 0.8 at 1.5 s, resulting in an actual postdisturbance grid impedance of $(2.45 + j12.25)$ Ω. After a short period of fitting process, the circle center converges to (0.154, 0.783), leading to an estimated grid impedance $(2.42 + j12.3)$ Ω, which closely matches the actual value with high accuracy.

D. Adaptation to Changed Grid Voltage

As discussed in Section III-F, the proposed method remains applicable even when the grid voltage is nonnominal during an SCR drop event. To validate this, simulation is conducted under such conditions, and the results are shown in Fig. 14. At 1.5 s, SCR drops to 0.8, accompanied by a grid voltage dip to 0.75 p.u. After the circle fitting process, the algorithm yields a stable output, with a fitted circle center of (0.11, 0.77) and a radius of 0.57. Based on the quasi-power circle fitting results, the estimated grid impedance is $(1.87 + j12.75)$ Ω, and new

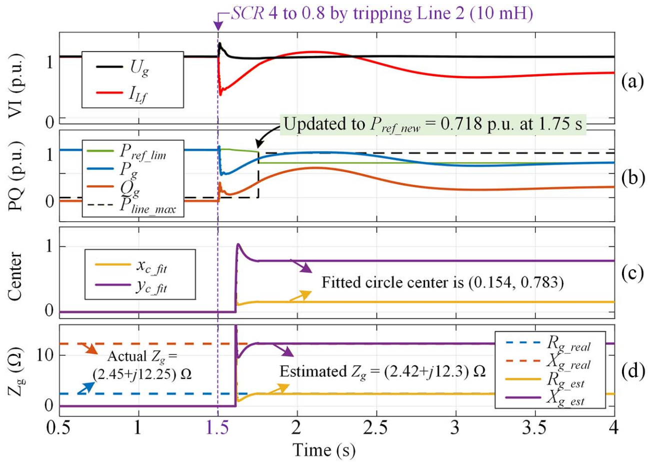

Fig. 13. Simulation results of grid-impedance estimation with grid impedance ratio R/X = 0.2: (a) magnitudes of PCC voltage and converter current; (b) limited active power reference, active and reactive power; (c) fitted circle center; and (d) actual and estimated grid impedance.

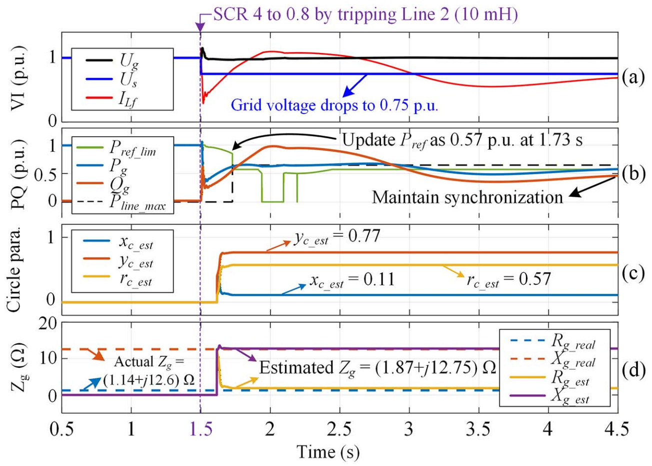

Fig. 14. Simulation results of grid-impedance estimation during a large SCR drop with a grid voltage dip to 0.75 p.u.: (a) magnitudes of PCC voltage, grid voltage, and converter current; (b) limited active power reference, active and reactive power; (c) fitted circle center and radius; and (d) actual and estimated grid impedance.

active power reference is determined to 0.57 p.u., ultimately ensuring stable system operation.

E. Comparison With Existing Method

Using the parameters listed in Table II and under the same disturbance of an SCR drop to 0.7, a comparison is made between the method presented in [7] and the proposed method. The results are shown in Figs. 15 and 16, respectively. At 1.5 s, the SCR drop occurs. The method in [7], which is based on the maximum active power detection, completes the grid impedance estimation at 1.89 s. However, even when the active power reference is updated using the same adjustment rule ($P_{\text{ref\_new}} = 0.85 \times P_{\text{line\_max}}$), the system still loses synchronization due to the limited angle stability margin. To maintain synchronization in this case, $P_{\text{ref\_new}}$ must be set even lower.

TABLE II
SYSTEM AND CONTROL PARAMETERS

Items	SI	Items	SI
Rated Power S_{rated}	1 kVA	Filter capacitance C_{sh}	30 μF
Line voltage U_{rated}	100 V	L_g (SCR = 4)	8 mH
Line frequency f_g	50 Hz	L_g (SCR = 0.8)	40 mH
DC voltage U_{DC}	300 V	R/X ratio	0.1
Rated current I_{rated}	10 A	Forgetting factor λ_{FF}	0.99
Filter inductance L_f	5 mH	Weight fact α_v	0.2

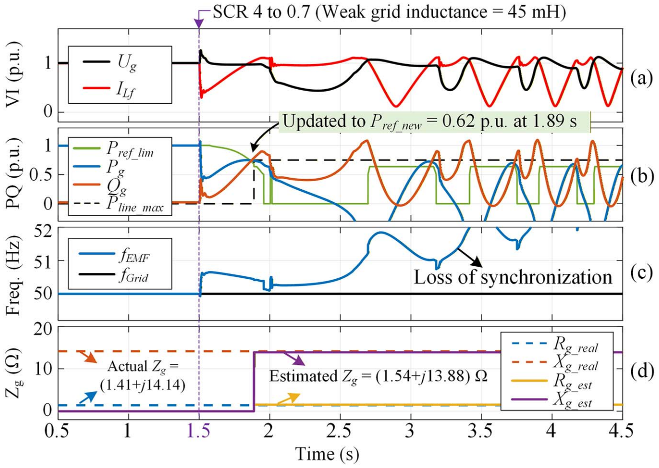

Fig. 15. Simulation results of grid-impedance estimation applying the method in [7]: (a) magnitudes of PCC voltage and converter current; (b) limited active power reference, active and reactive power; (c) frequency of GFM converter and the grid; and (d) actual and estimated grid impedance.

In contrast, the proposed method completes accurate estimation earlier, at 1.75 s. The active power reference is also adjusted to 0.85 × $P_{\text{line\_max}}$, yet the system remains stable. This improvement is due to the estimation being finalized before the operating point reaches the active power peak, providing more deceleration space to maintain synchronization. The proposed method offers faster, more accurate estimation and improved stability, demonstrating its practical value and necessity.

F. Converter Operation After SCR Recovery

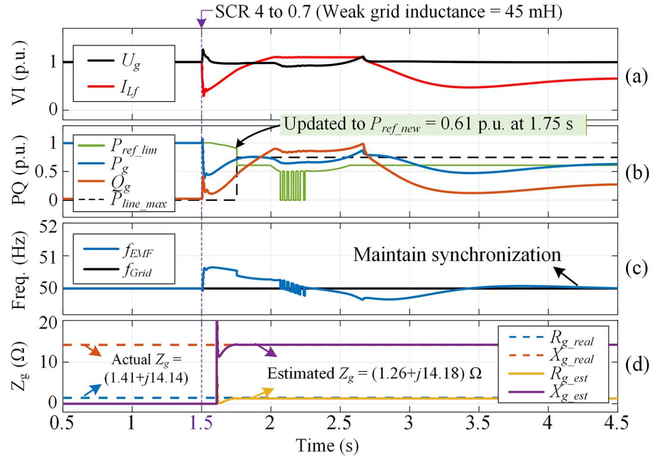

Fig. 16. Simulation results of grid-impedance estimation applying the proposed method: (a) magnitudes of PCC voltage and converter current; (b) limited active power reference, active and reactive power; (c) frequency of GFM converter and the grid; and (d) actual and estimated grid impedance.

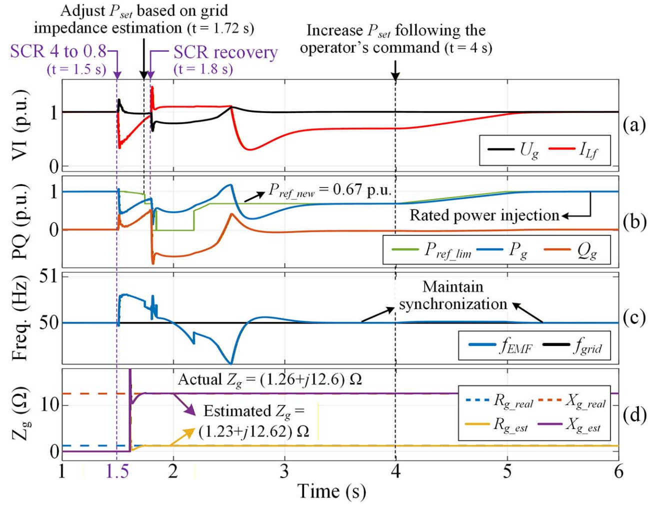

Fig. 17. Simulation results of grid-impedance estimation applying the proposed method during a short period SCR drop transient (0.3 s): (a) magnitudes of PCC voltage and converter current; (b) limited active power reference, active and reactive power; (c) frequency of GFM converter and the grid; and (d) actual and estimated grid impedance.

To evaluate the converter's performance when the tripped transmission line is reconnected after a short fault, a corresponding simulation is conducted, and the results are plotted in Fig. 17. The SCR drops at 1.5 s and restores at 1.8 s. Grid impedance estimation is completed at 1.72 s, updating the active power reference to 0.67 p.u. When the grid strength suddenly recovers, the converter current protection is triggered due to the relatively large power angle between PCC and the grid caused by the previous converter acceleration. After a brief resynchronization process, the converter reaches a steady state at around 3.3 s with reduced active power injection. Although the grid strength has been restored, maintaining synchronization is prioritized over immediately restoring nominal power output. Therefore, a gradual increase in active power delivery is recommended, following the grid operator's requirements. Assuming the grid operator issues a power ramp command at 4 s, the active power reference increases smoothly to nominal level, and by 5.2 s, the converter achieves steady-state operation with rated power delivery.

V. CONCLUSION

This article introduces an easily implemented passive grid impedance estimation method that relies solely on local measurements from a connected grid-forming (GFM) converter operating under ultraweak grid conditions. The proposed method determines both grid inductances and resistances by utilizing a fixed-centerd quasi-power circle, which effectively captures the natural relationship between active and reactive power changes at the PCC during transient events, regardless of grid frequency fluctuations. Furthermore, the constraints derived from the inherent physical characteristics of the power grid are integrated into the recursive least square (RLS)-based estimation algorithm to enhance the speed of the estimation process. The results of this estimation allow precise adjustments to the active power reference, enabling the GFM converter to maintain synchronization and continue injecting available power into the grid. Experimental validation confirms the method's reliability and accuracy.

REFERENCES

[1] R. Rosso, X. Wang, M. Liserre, X. Lu, and S. Engelken, "Grid forming converters: Control approaches, grid-synchronization, and future trends—A review," *IEEE Open J. Ind. Appl.*, vol. 2, pp. 93–109, 2021.

[2] T. Lund et al., "Operating wind power plants under weak grid conditions considering voltage stability constraints," *IEEE Trans. Power Electron.*, vol. 37, no. 12, pp. 15482–15492, Dec. 2022.

[3] C. Li, Y. Yang, Y. Cao, L. Wang, and F. Blaabjerg, "Frequency and voltage stability analysis of grid-forming virtual synchronous generator attached to weak grid," *IEEE J. Emerg. Sel. Top. Power Electron.*, vol. 10, no. 3, pp. 2662–2671, Jun. 2022.

[4] J. Erdocia, A. Urtasun, and L. Marroyo, "Power angle–frequency droop control to enhance transient stability of grid-forming inverters under voltage dips," *IEEE J. Emerg. Sel. Top. Power Electron.*, vol. 11, no. 4, pp. 3751–3764, Aug. 2023.

[5] A. Narula, P. Imgart, M. Bongiorno, M. Beza, J. R. Svensson, and J.-P. Hasler, "Voltage-based current limitation strategy to preserve grid-forming properties under severe grid disturbances," *IEEE Open J. Power Electron.*, vol. 4, pp. 176–188, 2023.

[6] D. Yang, X. Wang, F. Liu, K. Xin, Y. Liu, and F. Blaabjerg, "Adaptive reactive power control of PV power plants for improved power transfer capability under ultra-weak grid conditions," *IEEE Trans. Smart Grid*, vol. 10, no. 2, pp. 1269–1279, Mar. 2019.

[7] B. Pepper and D. Campos-Gaona, "Impedance estimation for transient stability enhancement of virtual synchronous machines," in *Proc. IEEE 15th Int. Symp. Power Electron. Distrib. Gener. Syst. (PEDG)*, Luxembourg, Luxembourg, 2024, pp. 1–6.

[8] M. K. De Meerendre, E. Prieto-Araujo, K. H. Ahmed, O. Gomis-Bellmunt, L. Xu, and A. Egea-Àlvarez, "Review of local network impedance estimation techniques," *IEEE Access*, vol. 8, pp. 213647–213661, 2020.

[9] N. Mohammed, M. H. Ravanji, W. Zhou, and B. Bahrani, "Online grid impedance estimation-based adaptive control of virtual synchronous generators considering strong and weak grid conditions," *IEEE Trans. Sustain. Energy*, vol. 14, no. 1, pp. 673–687, Jan. 2023.

[10] L. Asiminoaei, R. Teodorescu, F. Blaabjerg, and U. Borup, "A digital controlled PV-inverter with grid impedance estimation for ENS detection," *IEEE Trans. Power Electron.*, vol. 20, no. 6, pp. 1480–1490, Nov. 2005.

[11] D. K. Alves, R. L. d A. Ribeiro, F. B. Costa, T. d O. A. Rocha, and J. M. Guerrero, "Wavelet-based monitor for grid impedance estimation of three-phase networks," *IEEE Trans. Ind. Electron.*, vol. 68, no. 3, pp. 2564–2574, Mar. 2021.

[12] M. Céspedes and J. Sun, "Online grid impedance identification for adaptive control of grid-connected inverters," in *Proc. IEEE Energy Convers. Congr. Expo. (ECCE)*, Raleigh, NC, USA, 2012, pp. 914–921.

[13] N. Mohammed and M. Ciobotaru, "Fast and accurate grid impedance estimation approach for stability analysis of grid-connected inverters," *Electr. Power Syst. Res.*, vol. 207, 2022, Art. no. 107831.

[14] A. Suárez, C. Blanco, P. García, Á. Navarro-Rodríguez, and J. Manuel Cano Rodríguez, "Grid impedance estimator for active multisource AC grids," *IEEE Trans. Smart Grid*, vol. 14, no. 3, pp. 2023–2033, May 2023.

[15] P. García, M. Sumner, Á. Navarro-Rodríguez, J. M. Guerrero, and J. García, "Observer-based pulsed signal injection for grid impedance estimation in three-phase systems," *IEEE Trans. Ind. Electron.*, vol. 65, no. 10, pp. 7888–7899, Oct. 2018.

[16] S. Neshvad, S. Chatzinotas, and J. Sachau, "Wideband identification of power network parameters using pseudo-random binary sequences on power inverters," *IEEE Trans. Smart Grid*, vol. 6, no. 5, pp. 2293–2301, Sep. 2015.

[17] T. Roinila and T. Messo, "Online grid-impedance measurement using ternary-sequence injection," *IEEE Trans. Ind. Appl.*, vol. 54, no. 5, pp. 5097–5103, Sep./Oct. 2018.

[18] N. Mohammed, M. Ciobotaru, and G. Town, "Fundamental grid impedance estimation using grid-connected inverters: A comparison of two frequency-based estimation techniques," *IET Power Electron.*, vol. 13, no. 13, pp. 2730–2741, 2020.

[19] D. K. Alves, R. L. A. Ribeiro, F. B. Costa, and T. O. A. Rocha, "Real-time wavelet-based grid impedance estimation method," *IEEE Trans. Ind. Electron.*, vol. 66, no. 10, pp. 8263–8265, Oct. 2019.

[20] M. Ciobotaru, R. Teodorescu, P. Rodriguez, A. Timbus, and F. Blaabjerg, "Online grid impedance estimation for single-phase grid-connected systems using PQ variations," in *Proc. IEEE Annu. Power Electron. Specialists Conf. (PESC)*, Jun. 2007, pp. 2306–2312.

[21] N. Mohammed, T. Kerekes, and M. Ciobotaru, "An online event-based grid impedance estimation technique using grid-connected inverters," *IEEE Trans. Power Electron.*, vol. 36, no. 5, pp. 6106–6117, May 2021.

[22] R. Fantino et al., "Grid impedance estimation by measuring only the current injected to the grid by a VSI with LCL filter," *IEEE Trans. Ind. Electron.*, vol. 68, no. 3, pp. 1841–1850, Mar. 2021.

[23] J. Sun, J. Yu, J. Qiu, and Y. Wang, "Transient-responses-based grid impedance estimation for grid-forming converters," in *Proc. 4th Int. Conf. Elect. Eng. Control Technol.*, 2022, pp. 741–745.

[24] J. Fang, H. Deng, and S. M. Goetz, "Grid impedance estimation through grid-forming power converters," *IEEE Trans. Power Electron.*, vol. 36, no. 2, pp. 2094–2104, Feb. 2021.

[25] N. Hoffmann and F. Fuchs, "Minimal invasive equivalent grid impedance estimation in inductive-resistive power networks using extended Kalman filter," *IEEE Trans. Power Electron.*, vol. 29, no. 2, pp. 631–641, Feb. 2014.

[26] J. Ye, Z. Zhang, A. Shen, J. Xu, and F. Wu, "Kalman filter based grid impedance estimating for harmonic order scheduling method of active power filter with output LCL filter," in *Proc. Int. Symp. Power Electron., Electr. Drives, Autom. Motion (SPEEDAM)*, Jun. 2016, pp. 359–364.

[27] S. Zhao and S. K. Sul, "Real-time grid parameter estimation with grid-forming converters for robust synchronous power control," *J. Power Electron.*, vol. 24, pp. 159–170, 2024.

[28] M. Beza and M. Bongiorno, "A modified RLS algorithm for online estimation of low-frequency oscillations in power systems," *IEEE Trans. Power Syst.*, vol. 31, no. 3, pp. 1703–1714, May 2016.

[29] S. Liu et al., "Islanding detection method based on system identification," *IET Power Electron.*, vol. 9, no. 10, pp. 2095–2102, 2016.

[30] P. Me, S. Zabihi, F. Blaabjerg, and B. Bahrani, "adaptive virtual resistance for postfault oscillation damping in grid-forming inverters," *IEEE Trans. Power Electron.*, vol. 37, no. 4, pp. 3813–3824, Apr. 2022.

Wentao Liu (Member, IEEE) received the B.S. degree in electrical engineering and automation and the M.S. degree in electrical engineering from Shandong University, Jinan, China, in 2018 and 2020, respectively, and the Ph.D. degree in power electronics from AAU Energy, Aalborg University, Aalborg, Denmark, in 2024.

He is currently a Postdoctoral Researcher with the Department of Electric Power Engineering, Chalmers University of Technology, Gothenburg, Sweden. His research interests include the modeling and control of grid-forming (GFM) converters, grid stability assessment, grid impedance estimation, and wide bandgap power devices.

Massimo Bongiorno (Senior Member, IEEE) received the M.Sc. degree in electrical engineering from the University of Palermo, Palermo, Italy, in 2002, and the Lic. Eng. and Ph.D. degrees in electric power engineering from Chalmers University of Technology, Gothenburg, Sweden, in 2004 and 2007, respectively.

Since 2015, he has been a Professor in power electronic applications for power systems and, since 2020, the Head of the Division of Electric Power Engineering, Chalmers University of Technology. Since 2022, he has been the Director of the Centre of Excellence, Swedish Electricity Storage and Balancing Centre. From 2007 to 2010, he was an Assistant Professor with the Department of Electric Power Engineering, Chalmers University of Technology, where he became an Associate Professor in 2010. His research interests include the application of power electronics in power systems, converter control, power system dynamics, and power quality.

Anant Narula received the M.Sc. degree in Smart Electrical Networks and Systems in 2018 as part of the joint master's program (EIT InnoEnergy) from the KTH Royal Institute of Technology, Stockholm, Sweden, and the Universitat Politècnica de Catalunya, Barcelona, Spain, and the Ph.D. degree in electric power engineering from Chalmers University of Technology, Gothenburg, Sweden, in 2023.

He is currently a Research Specialist with the Department of Electrical Engineering, Chalmers University of Technology. His research interests include applications of power electronics in power systems, converter control, and power system stability.

Jan R. Svensson (Senior Member, IEEE) received the Ph.D. and D.Sc. degrees (Docent) in electric power engineering from Chalmers University of Technology, Göteborg, Sweden, in 1998 and 2002, respectively.

He is currently a Research Fellow with Hitachi Energy Research, Västerås, Sweden. Since 2018, he has been an Adjunct Professor with Chalmers University of Technology. From 1999 to 2009, he was with ABB, Västerås, Sweden, in R&D of HVDC transmission, STATCOMs, and energy storages, especially design and control of Light-concept devices (HVDC and FACTS). From 2009 to 2014, he was the Program Manager for the Global R&D Program "Active Grid Infrastructure" with ABB Corporate Research, Västerås, Sweden. From 2014 to 2020, he was a Senior Principal Scientist on power electronics systems with ABB Corporate Research. His research interests include design and control of power electronics in power systems, power quality, storage technologies, and renewable energy.